scientific reports

Check for updates

OPEN

Biodegradable zinc alloys with high strength and suitable mechanical integrity as bone repair metals

Chengwu Lu[1,4,5], Chao Song[1,2,3,5], Yunlong Yu[1,2,3,5], Linhai Yang[1,2], Wu Zheng[1,2,3], Fenqi Luo[1,2,3], Yuhua Xiao[1,2,3], Jun Luo[1,2,3]✉ & Jie Xu[1,2,3]✉

Mechanical properties and integrity of biodegradable Zn alloys during degradation holds significant importance. In this study, a Zn-Mg-Mn alloy with tensile strength of 414 MPa and an elongation of 26% was developed. The strength contributions of as-extruded Zn alloy from grain boundary strengthening, precipitation strengthening, and second phase strengthening. Degradation of the Zn alloy in Hank's solution exhibited a decreasing trend with prolonged immersion, eventually stabilizing at 16 μm/year. Corrosion morphology analysis revealed that the corrosion modes transformed from pitting corrosion to severely localized corrosion with prolonged immersion time, eventually lead to formation of large holes. Although the tensile strength of the Zn alloys remained relatively unchanged following varied immersion time, a substantial decrease in elongation was observed. The decreased elongation primarily attributed to the formation of surface corrosion pits or holes, exacerbating crack propagation during tension. Biocompatibility assessments of Zn alloys demonstrated that a 50% concentration of Zn alloy leach solution cultured with C3H10 and RMSC cells yielded cellular activity exceeding 80%, indicating excellent cytocompatibility. Alkaline phosphatase (ALP) and alizarin red staining results further underscored the remarkable early and late osteogenic properties exhibited by Zn-Mg-Mn alloy.

Keywords Biodegradable zn alloys, Mechanical properties, Mechanical integrity, Biocompatibility

In recent years, biodegradable zinc (Zn) alloys hold immense promise for biomedical applications[1,2]. On the one hand, Zn exhibits a moderate degradation rate in the human environment, generating non-toxic by-products and avoiding high pH values in local microenvironments[3–6]. On the other hand, Zn serves as an essential trace element in the human body, primarily distributed in bones and muscles, participating in biochemical reactions[7]. Although degradability and biocompatibility of Zn are appropriate, its mechanical properties are also key due to support function of biodegradable metals. For instance, ultimate tensile strength (UTS) of biodegradable Mg stents requires over 300 MPa[8]. This requirement limits the application of biodegradable pure Zn, which has strength lower than 200 MPa[9,10]. To improve strength of pure Zn, alloying with other non-toxic elements is effectively. Strength improvements of Zn alloys are achieved through solid solution strengthening, precipitation strengthening, modulus strengthening by second phase, and dislocation strengthening[11–13]. These strengthening mechanisms bring different strength contributions depending on the chemical compositions and processing methods.

With the development of Zn alloys, magnesium (Mg) is verified as a better strengthening element due to the formation of lamellar eutectic structure in Zn-Mg alloys[14–16]. The strength improvement is demonstrated as increasing the fraction of eutectic structure. For instance, Mostaed et al. observed a rise in tensile strength from 250 to 399 MPa with increasing Mg content from 0.15 wt% to 3 wt%[17]. Wang et al. corroborated this finding, demonstrating increased tensile strength in Zn-Mg alloys with rising Mg content, even after extrusion at different temperatures[18]. Furthermore, addition of Mg element significantly promotes grain refinement induced by dynamically recrystallized (DRX). After hydrostatic extrusion, the average grain size of Zn is reduced to 700 nm, resulting in a high strength of 435 MPa and elongation of 35%. Apart from fine Zn grains, the complete refinement of eutectic is crucial for the mechanical properties, as reported the Zn-1.6Mg alloys with strength of 474 MPa processed by equal channel angular pressing (ECAP)[19].

[1]Shengli Clinical Medical College of Fujian Medical University, Fuzhou 350000, China. [2]Department of Orthopedics, Fujian Provincial Hospital, Fujian Medical University, Fuzhou 350000, China. [3]Fuzhou University Affiliated Provincial Hospital, Fuzhou 350000, China. [4]Nanping First Hospital Affiliated to Fujian Medical University, Nanping 353000, China. [5]Chengwu Lu, Chao Song and Yunlong Yu have considered joint first author. ✉email: 18634835@qq.com; jiexu1520@163.com

However, the increased fraction of eutectic structure makes it hard to full refinement by extrusion or rolling processes, leading to low elongations. Although severe plastic deformation can effectively refine eutectic structure, the Zn/Mg_2Zn_{11}interface becomes more activated and thereby reduces strength[13]. Moreover, the incomplete refinement of eutectic structure after thermomechanical properties impacts corrosion behaviors due to the low standard electrode potential of Mg[20,21]. Localized corrosion is observed in as-cast Zn-Mg alloys and becomes more severe as increasing Mg content[22]. Thus, selecting an appropriate Mg content in Zn-Mg based alloys is necessary to balance strength and elongation, mitigate the localized corrosion at the same time. Previous studies have demonstrated that the elongation is significantly reduced when Mg content exceeds 1 wt% in Zn-Mg alloys[17,18]. Kubásek et al. found that as-extruded Zn-0.8Mg wt% alloy has a moderate elongation (13%), with strength of 300 MPa[23]. Consequently, we finally decided that Mg content is 0.8 wt% after balancing mechanical properties.

On the basis of binary Zn-Mg alloys, adding the third element is a better choice for compensating strength loss from decreasing Mg content. Apart from Mg, manganese (Mn) is also beneficial to mechanical properties, especially to elongation. The reported Zn-Mn alloys have high elongations, which is attributed to the fine grains (<5 μm) and twinning deformation in $MnZn_{13}$phase[24–26]. At present, addition of Mn into Zn-Mg alloys has been developed, resulting in good elongations ($>20\%$)[27,28]. Although the developed Zn-Mg-Mn alloys also have moderate strengths, the loss of mechanical properties during immersion have not been investigated. For degradable metals, Zn alloys must meet specific degradation rate criteria in vivo, maintaining uniform degradation in early service to ensure mechanical property stability[29]. Hence, this study designed a Zn-Mg based alloy with strength-plasticity to elucidate Zn alloy mechanical stability as a degradable metal in body fluid environments by examining mechanical property changes following various immersion cycles.

Experimental procedure

The chemical composition of Zn alloy in this study was designed as Zn-0.8Mg-0.2Mn (wt%). Pure Zn (99.99 wt%), pure Mg (99.99 wt%), and pure Mn (99.95 wt%) were melted at 550 °C under vacuum in a melting furnace, then poured into preheated molds to obtain the as-cast alloy. The actual composition, determined by Inductively Coupled Plasma-Mass Spectrometry (ICP-MS), was Zn-0.78Mg-0.21Mn (wt%). Cylinder billets with a diameter of 60 mm and height of 40 mm, were cut from the ingot and then extruded at 150 °C to produce a final extruded bar with a diameter of 10 mm. Extrusion parameters included a speed of 1 mm/s and extrusion ratio of 36:1. Squares measuring 8 mm in length, 6 mm in width, and 2 mm in thickness were cut from both the as-cast and extruded Zn alloys for microstructure analysis. The direction of length is parallel to extrusion direction. Microstructural observation utilized a scanning electron microscope (SEM: SU8220, Hitachi, Japan) equipped with GENESIS 60 S X-ray energy spectrometer (EDS) (QUANTAX FlatQUAD, Bruker, America). Before observation, samples were mechanically grinded by SiC papers and then polished to mirror surface. The prepared samples were etched using 4 vol% HNO_3 + alcohol solution. In order to obtain grain size distribution and dislocation density, electron backscatter diffraction (EBSD: Nanoanalysis, Oxford, England) was conducted. The grinded samples were polished on an argon (Ar) ion milling system. A transmission electron microscope (TEM: Talos F200X, Thermo Fisher Scientific, USA) were used to observe refined eutectic structure and fine $MnZn_{13}$ phase. The thickness of samples was reduced to below 100 μm by mechanically grinding. The thin samples were twin-jet electron-polished in the 5 wt% perchloric acid alcohol solution. Quasi-static tensile tests were conducted at room temperature on dog-bone-shaped plates measuring 10 mm in length, 3 mm in width, and 2 mm in thickness, with a strain rate of 10^{-3} s^{-1} (Instron 5969, USA). To obtain elastic modulus of alloys, an extensometer (YSJ, Germany) was equipped with tension machinery.

Electrochemical experiments were carried out using a classical three-electrode electrochemical workstation (CHI600E). Three electrodes are working electrode (samples), a reference electrode (saturated calomel electrode (SCE)), and a counter electrode (platinum electrode), respectively. Open-circuit potential was measured for 3600 s, followed by Potentiodynamic polarization (PDP) curve was conducted over a voltage range from − 1.6 V vs. SCE to -0.8 V vs. SCE at a scanning rate of 0.1 mV/s. Samples underwent electrochemical and immersion experiments in Hank's solution for 7, 30, 90, and 180 days. After immersion, Zn-Mg-Mn alloys were treated with a CrO_3 solution (200 g/L) to remove surface corrosion products, following by washing in distilled water and then dried.

Osteogenesis plays an important role in skeletal development and bone fracture healing. Thus, cytotoxicity experiments utilized mouse mesenchymal stem (C3H10) cells and rat mesenchymal stem cells (RMSC), which were sourced from American Type Culture Collection (ATCC). They were cultured in α-MEM with 10% fetal bovine serum (FBS) and 1% penicillin-streptomycin at 37 °C, 95% humidity, and 5% CO_2. Medium renewal occurred every two days. Samples underwent ultrasonic cleaning, sterilization under UV light for a minimum of 4 h, and irradiation of each surface. The medium-to-surface area ratio was 1.25 mL/cm^2. Following soaking, extracts were collected, centrifuged, and stored at 4 °C.

For trypsinization, detached cells were treated with four times the volume of trypsinized serum-containing medium. The digested medium was centrifuged, top liquid discarded, and fresh medium added, diluting cells to 3×10^4 cells/mL. Cells were seeded into 96-well plates, incubated for 24 h, then exposed to 100 μL of metallic material extract (experimental group) or inert metal Ti (control). Extract or control medium was refreshed every 48 h for testing 100% and 50% extract concentrations, respectively. Each extract was tested in five wells. Cytotoxicity assessments were conducted after 3 and 7 days of cell incubation. Absorbance tests at 450 nm were performed using a Bio-RAD680 microplate reader after 1-hour incubation. The relative cell proliferation rate was calculated.

For Alkaline phosphatase (ALP) and alizarin red staining (ARS), cells were cultured similarly. Extracts were diluted to 50% based on staining results and prepared as osteo-inductive solutions. The induction process spanned 3, 7, and 14 days, with medium renewal every 48 h.

Results

Figure 1 illustrates the microstructures of both as-cast and as-extruded Zn alloys. In the as-cast state, Zn grains appear irregularly shaped and exceed 50 μm in size. These grains are interspersed with numerous second phases arranged in a lamellar structure (highlighted in white circles in Fig. 1a). This lamellar structure, a typical feature of eutectic phase in Zn-Mg based alloys, alternates between Zn grains and Mg_2Zn_{11}phases, consistent with prior literature[17]. After extrusion, grain sizes were significantly reduced, rendering them equiaxed in morphology. Furthermore, the lamellar second phase in the as-cast alloy transforms into a granular phase, noticeably smaller than the Zn grains (as depicted in Fig. 1b). Transmission electron microscopy (TEM) analysis of the fine grain region reveals dynamically recrystallized (DRX) grains with high-angle grain boundaries separating adjacent grains (Fig. 1c). Within the fine eutectic microstructure particle phase, numerous nano-sized phases are observed (Fig. 1d). Previous research by Liu et al. identified these nanophases in the Mg_2Zn_{11} phase as $MgZn_2$phases[30]. Although trace amounts of Mn are undetectable under SEM, TEM reveals abundant nano-sized precipitates at grain boundaries of the fine grains (Fig. 1e). Thus, the microstructure of the as-extruded Zn-Mg-Mn alloy comprises fine DRX grains, granular Mg_2Zn_{11} phase, nano-sized $MgZn_2$ phase, and $MnZn_{13}$ phase.

Figure 2 presents the EBSD results for the as-extruded Zn alloy. The grain orientation colors exhibit uniform distribution in three different directions, indicating relatively weak texture in the as-extruded Zn alloy. Due to Zn alloys' low melting point, the extrusion temperature surpasses the DRX temperature of Zn components significantly. Consequently, no distinct preference for a recrystallization texture composed of DRX grains is evident. Grain size distribution histogram reveals an average grain size of 4.58 μm in the as-extruded Zn alloy. Additionally, assessment of dislocation density through local average misorientation mapping according to the equation: $\rho = 2\theta/\mu b$, where θ, μ, and b are LAM value, step size (0.5 μm), and Burgers vector of Zn (0.267 nm). It indicates an average misorientation of 0.46° and a calculated density of geometrically necessary dislocation (GND) at $1.36 \times 10^{14}/m^2$. The low dislocation density primarily stems from continuous DRX process in the Zn alloy, wherein resulting dislocations transition into low-angle grain boundaries and subsequently convert into high-angle grain boundaries in subsequent processing steps.

The mechanical properties of the as-cast and as-extruded Zn alloy are illustrated in Fig. 3. The tensile curve reveals two distinct phases: elastic deformation and plastic deformation at room temperature. In the elastic phase, stress rises linearly with strain. Subsequently, in the plastic deformation phase, stress peaks and then gradually decreases with increasing strain. The tensile yield strength (YS), UTS, and elongation of the as-cast Zn alloy measure 148 MPa, 168 MPa, and 2%, respectively. They increased to 342 MPa, 414 MPa, and 26%, respectively. These properties surpass the mechanical requirements for biodegradable metals, with YS > 200 MPa,

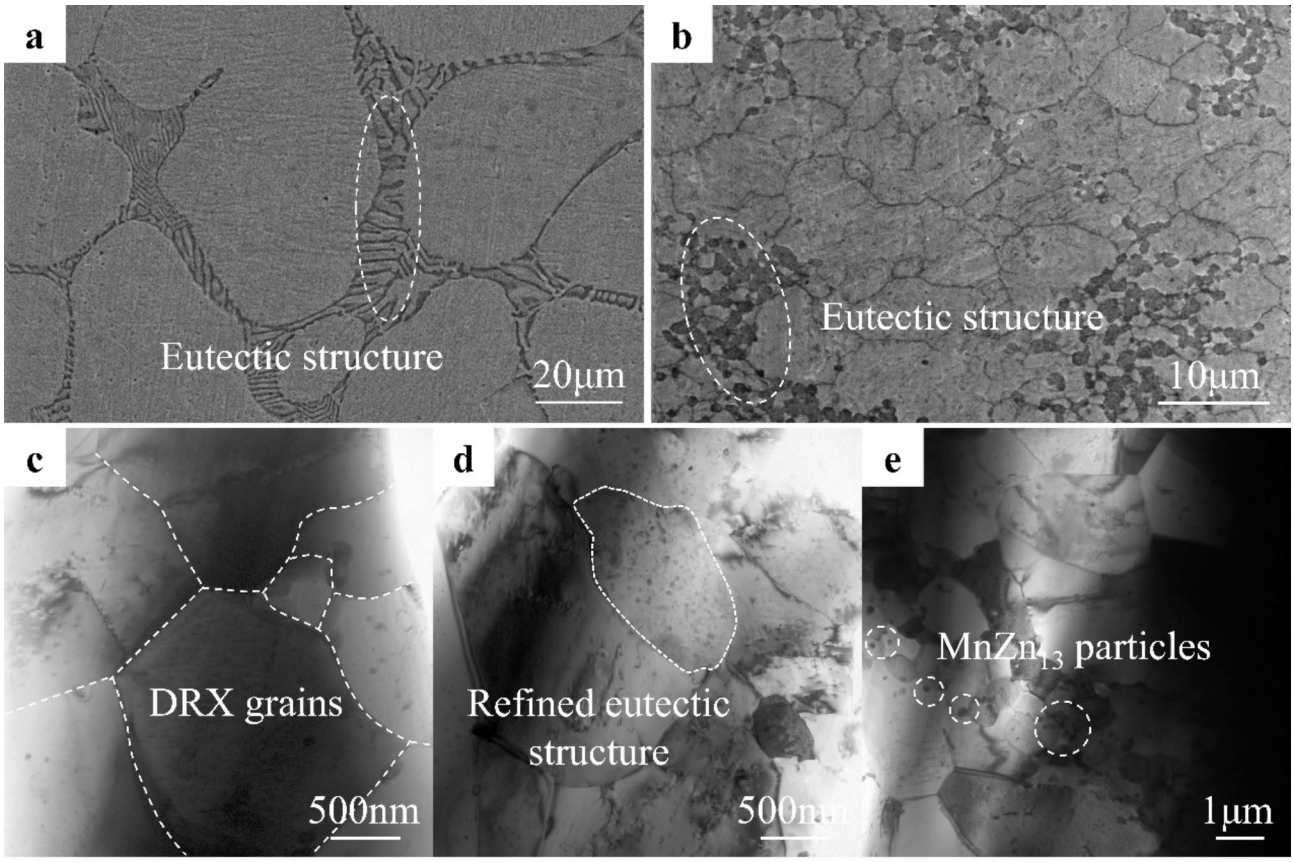

Fig. 1. Microstructures of Zn alloys. (**a**) SEM image of as-cast Zn alloys. (**b**) SEM image of as-extruded Zn alloys. TEM images of (**c**) DRX grains, (**d**) refined eutectic structure, and (**e**) $MnZn_{13}$ particles.

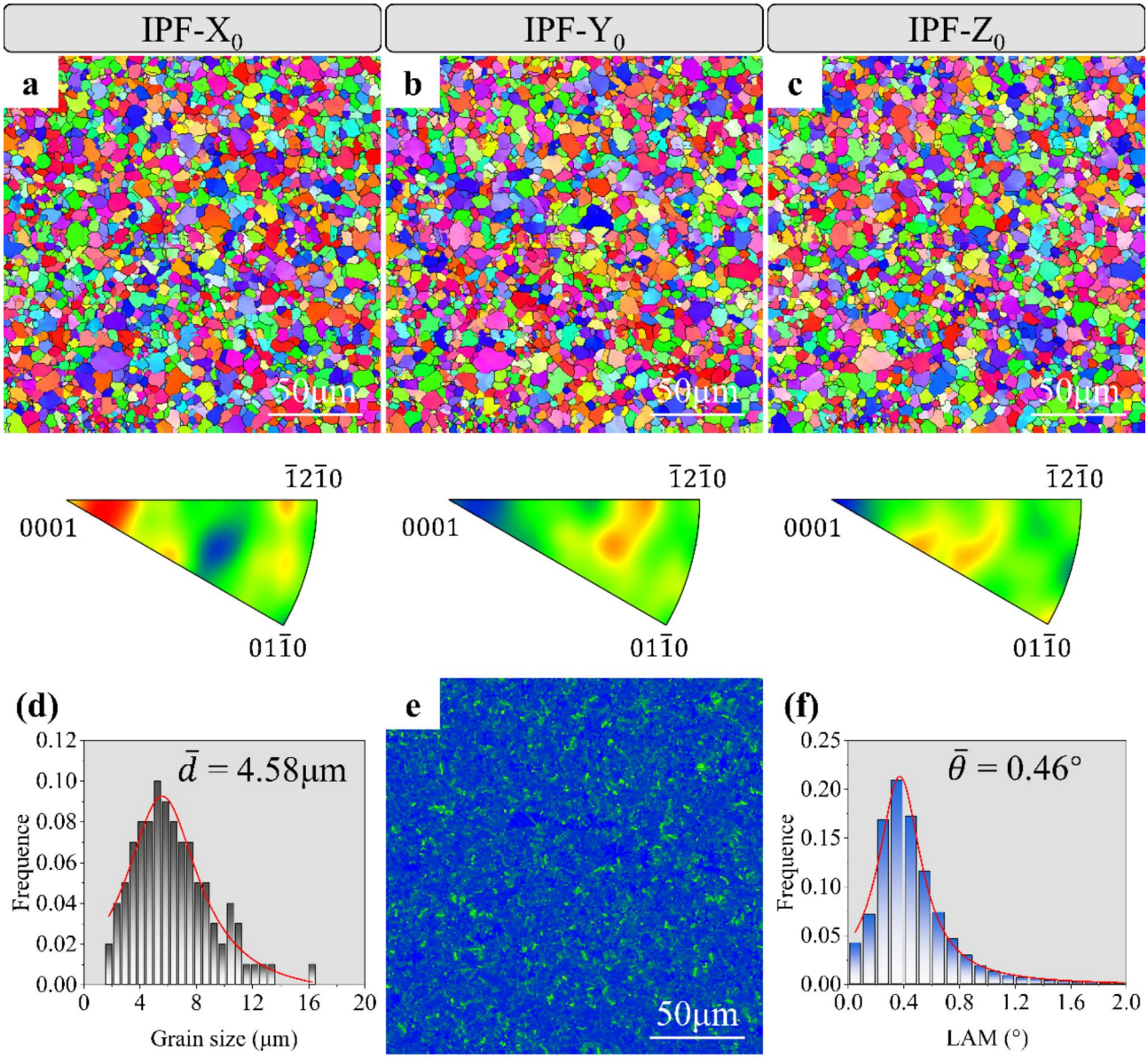

Fig. 2. EBSD analysis of as-extruded Zn alloys. (**a**) IPF-X_0 images. (**b**) IPF-Y_0 images. (**c**) IPF-Z_0 images. (**d**) Grain size distribution. (**e**) KAM image. (**f**) Local misorientation distribution.

UTS > 300 MPa, and elongation > 15%[31]. Moreover, the elastic modulus of the as-extruded Zn alloy was 95 GPa, which was obtained by linear fitting of the elastic stage.

Figure 4 displays the corrosion behaviors of as-extruded Zn alloys following various immersion cycles in Hank's solution. Electrochemical test results exhibit nearly overlapping kinetic potential polarization curves for Zn alloys subjected to different immersion durations. The corrosion potential and corrosion current density, that are obtained from PDP curves, of Zn alloys are listed in Table 1. The corrosion potential of as-extruded Zn alloy measures − 1.27 V vs. SCE, decreasing to approximately − 1.3 V vs. SCE after over 30 days of immersion. Corrosion current densities (i_{corr}) for all four Zn alloy variants approximate 1.7×10^{-6} A/cm^2. The corrosion rate (C, μm/year) is calculated from i_{corr} according to the equation: $C = \frac{3.3 i_{corr} E.W.}{n\rho}$, where n, E.W., and ρ are loss number of electrons (2), equivalent weight (64.7) and density (7.1 g/cm^3), respectively[32]. The decreased i_{corr} values mean that corrosion rate decreased with increasing immersion time. Immersion experiment findings indicate elevated corrosion rates in the initial immersion stages, exceeding 30 μm/year. However, corrosion rates decrease over time, eventually stabilizing. The prolonged immersion yields a consistent corrosion rate of 16 μm/year.

Figure 5 depicts the corrosion morphology of the as-extruded Zn alloys immersed in Hank's solution for varying durations. After 7 days, numerous white corrosion particles emerge on the Zn alloy surface. Dark areas exhibit corrosion layer coverage, accompanied by micro-cracks within localized regions of the layer. With

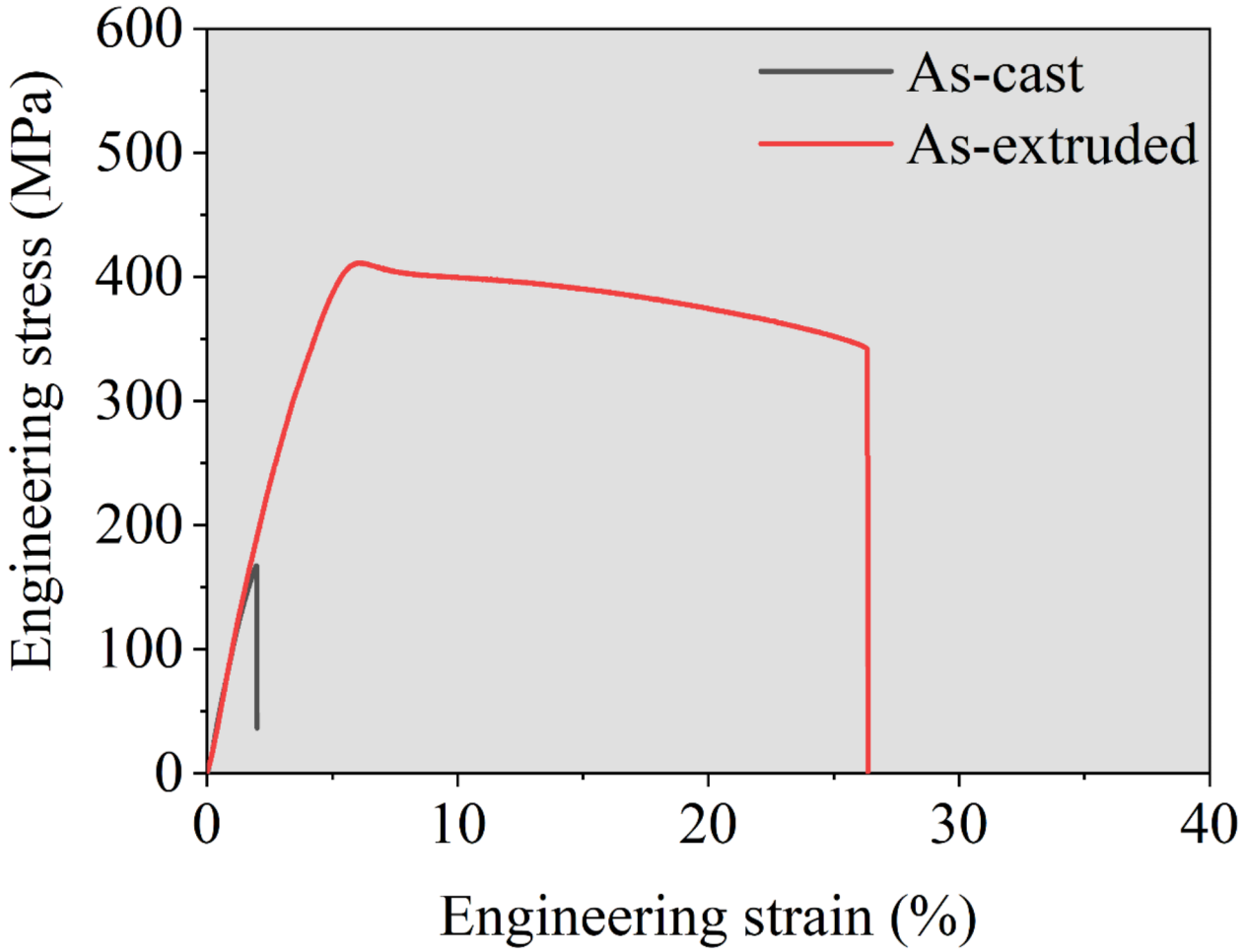

Fig. 3. Mechanical behavior of as-cast and as-extruded Zn alloy.

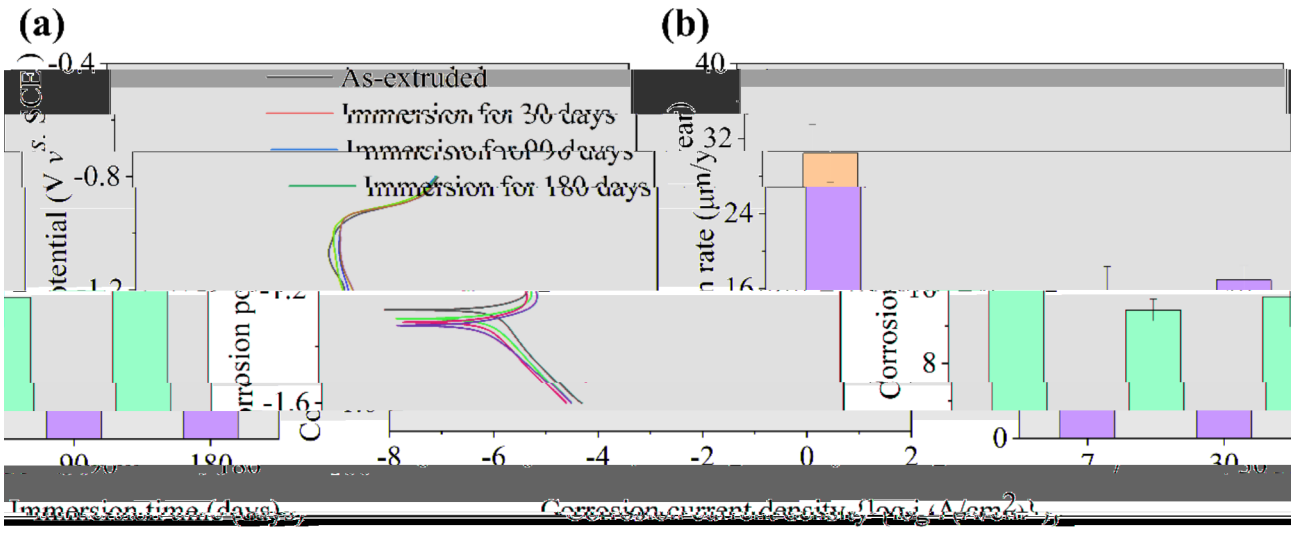

Fig. 4. Degradation behavior of as-extruded Zn alloys. (**a**) PDP curves. (**b**) Corrosion rate calculated from weight loss.

Samples	Corrosion potential (V. vs. SCE)	Corrosion current density
As-extruded	-1.27	1.95×10^{-5} (A/cm^2)
Immersion for 30 days	-1.31	1.91×10^{-5} (A/cm^2)
Immersion for 90 days	-1.32	1.66×10^{-5} (A/cm^2)
Immersion for 180 days	-1.32	1.78×10^{-5} (A/cm^2)

Table 1. Corrosion potential and corrosion current density of Zn alloys are obtained from PDP curves.

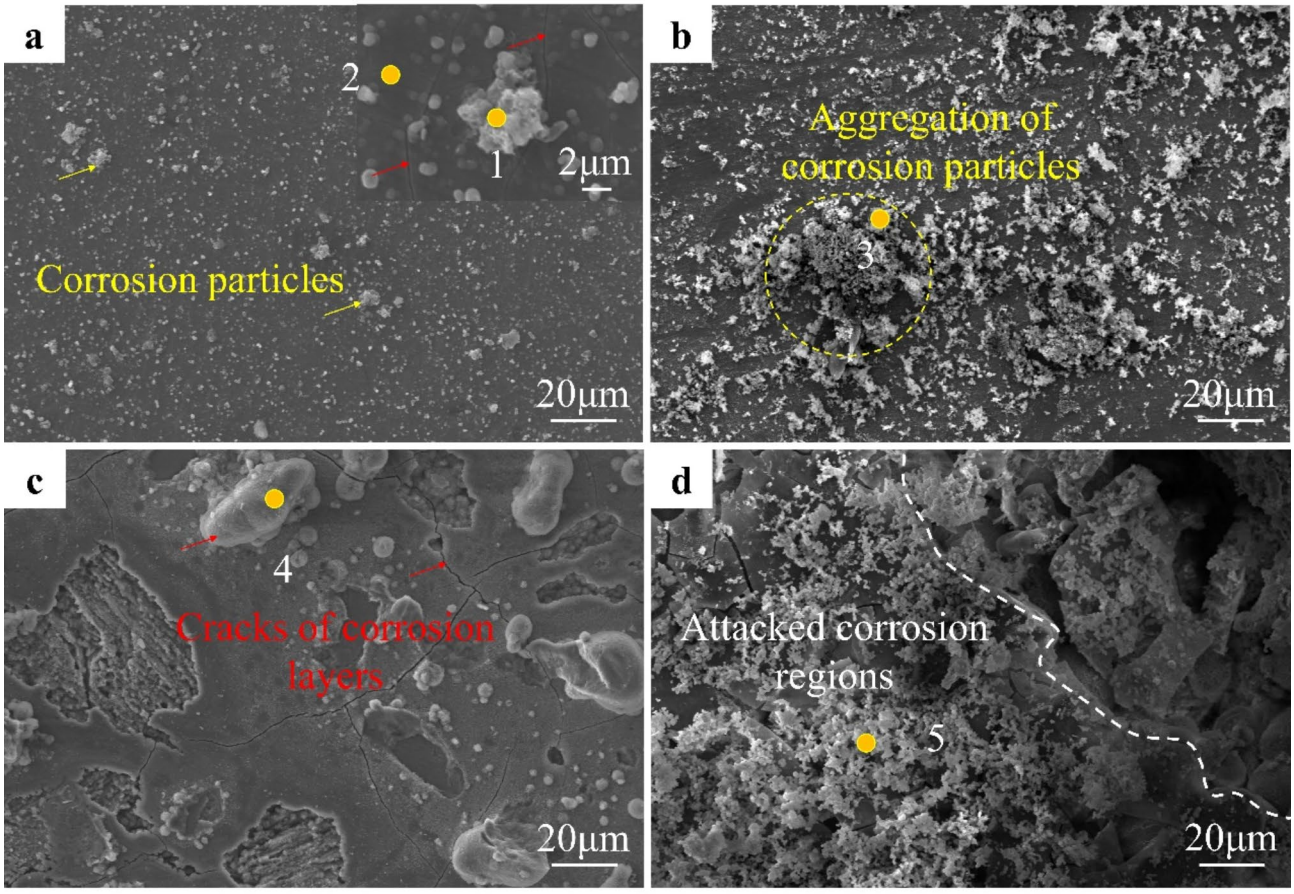

Fig. 5. Corrosion morphology of as-extruded Zn alloys before removing corrosion products. (**a**) Immersion for 7 days. (**b**) Immersion for 30 days. (**c**) Immersion for 90 days. (d) Immersion for 180 days.

Areas	Chemical compositions (wt%)					
	C	O	*P*	Mg	Ca	Zn
1	4.11	19.92	0.39	2.40	0.30	72.88
2	5.68	4.29	0.40	2.56	0.20	86.87
3	3.98	21.17	0.41	2.53	0.21	71.70
4	4.25	18.17	0.38	2.71	0.31	74.18
5	5.12	20.09	0.42	2.65	0.28	71.44

Table 2. Chemical compositions of corrosion products.

prolonged immersion, the density of white corrosion particles increases, aggregating into large clusters. By the 90-day mark, larger corrosive particles become evident, alongside an expanded area of surface corrosion layer cracking and peeling. Following 180 days of immersion, corrosion product density escalates further, leading to localized corrosion pit formation upon subsequent corrosion layer peeling. EDS results, as shown in Table 2, indicate significantly high C and O content in the corrosion products. The C originated from the carbanion,

which deposited on the surface of Zn alloys. According to Fourier transform infrared spectra of Zn-Mg-Mn alloy, the presence of O is attributed to the hydroxide ion, carbanion, and phosphate anion[33]. In addition, the detected Ca and P in corrosion products may come from Ca ion and phosphate anion in Hank's solution.

Following the removal of corrosion products, the surface morphology of the Zn alloy is further examined, as depicted in Fig. 6. After 7 days of immersion, no significant corrosion pits are evident on the alloy surface. By the 30-day mark, small corrosion pits, each less than 10 μm in diameter, begin to emerge (as indicated by the white arrow in Fig. 6b). Subsequently, after 90 days of immersion, the number of corrosion pits escalates, with some merging to form localized corrosion zones (indicated by the white circles in Fig. 6c). After 180 days of immersion, the alloy surface exhibits extensive destruction, characterized by localized corrosion zones and numerous large-sized corrosion pits. These pits in number and size continue to increase with immersion time, ultimately leading to complete degradation post-service.

The immersion process induces significant surface morphology alterations in the Zn alloy, notably the formation of pitting craters resulting from local corrosion. This phenomenon significantly impacts the mechanical properties of Zn alloys. Figure 7 illustrates the tensile properties of the Zn alloy at room temperature following immersion for various durations. The results indicate insignificant changes in tensile strength during immersion, while elongation decreases with increased immersion time. Elongation reduction correlates with crack propagation, as corrosion pit craters on the surface serve as strain concentration sites during tensile loading. With increasing strain, cracks propagate within the alloy, ultimately leading to material failure. Prolonged soaking results in increased number and size of corrosion pits, exacerbating elongation degradation of the Zn alloy during immersion.

The results of cell activity, depicted in Fig. 8, were obtained by cultivating C3H10 and RMSC cells with varying concentrations of Ti and Zn alloy extracts. The inert Ti is not degraded, so proliferation and differentiation of cells are not affected by release of metallic ions. The undiluted and diluted Ti extracts showed good cytocompatibility for both C3H10 and RMSC cells. Notably, the undiluted Zn alloy extract exhibited poor cytocompatibility, with cell activity below 60% for both cell types. However, upon diluting the extract to 50%, a significant improvement in cytocompatibility was observed, with cell activity exceeding 80%. Additionally, incubation time had a minimal effect on cell activity. Specifically, for C3H10 cells, both 100% and 50% concentrations of the extract demonstrated an increase in cell activity with prolonged incubation. In contrast, RMSC cells cultured with the 100% concentration showed higher cell activity after 7 days compared to 3 days, but at 50% concentration, the

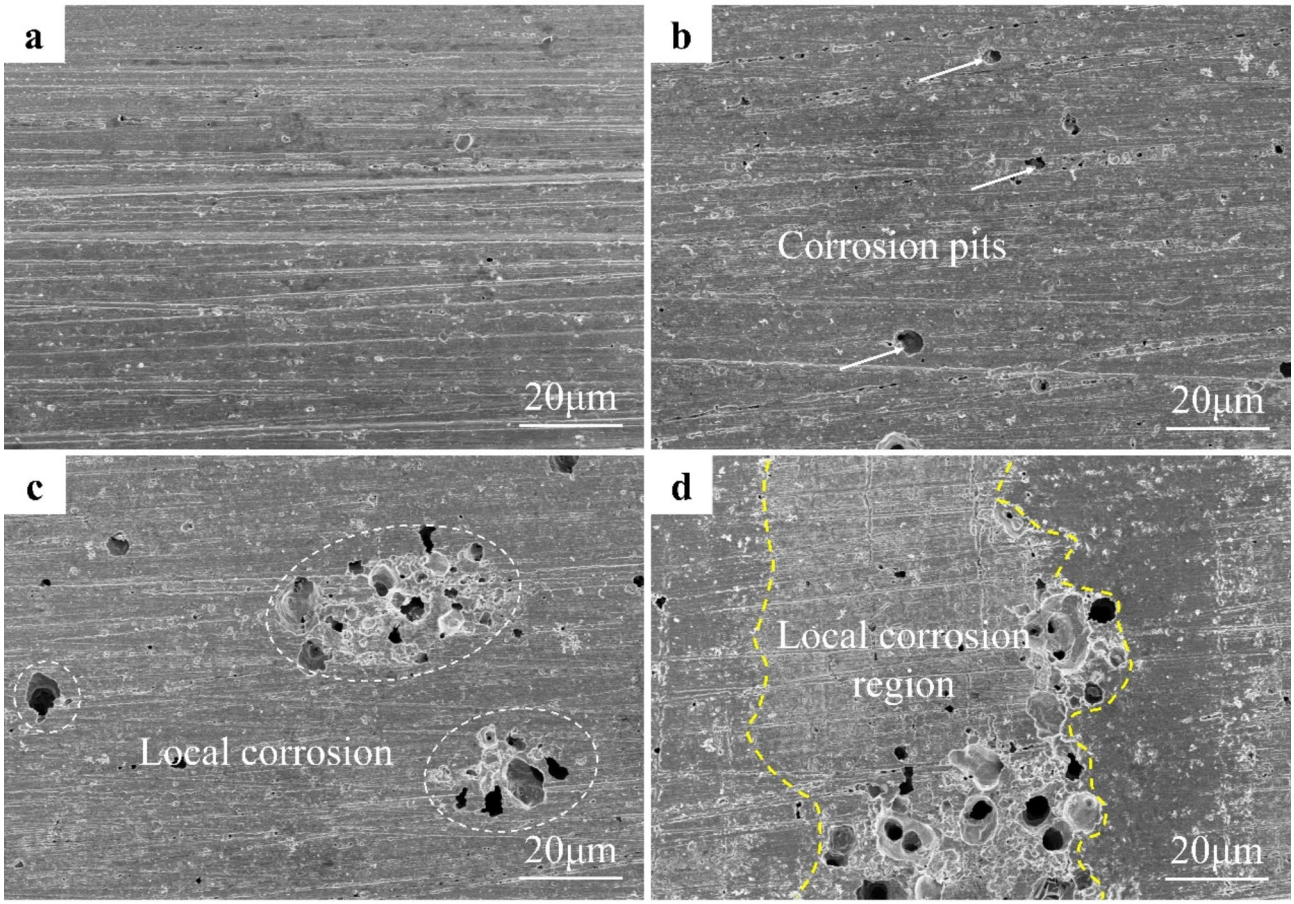

Fig. 6. SEM images of as-extruded Zn alloys after removing corrosion products. (**a**) Immersion for 7 days. (**b**) Immersion for 30 days. (**c**) Immersion for 90 days. (**d**) Immersion for 180 days.

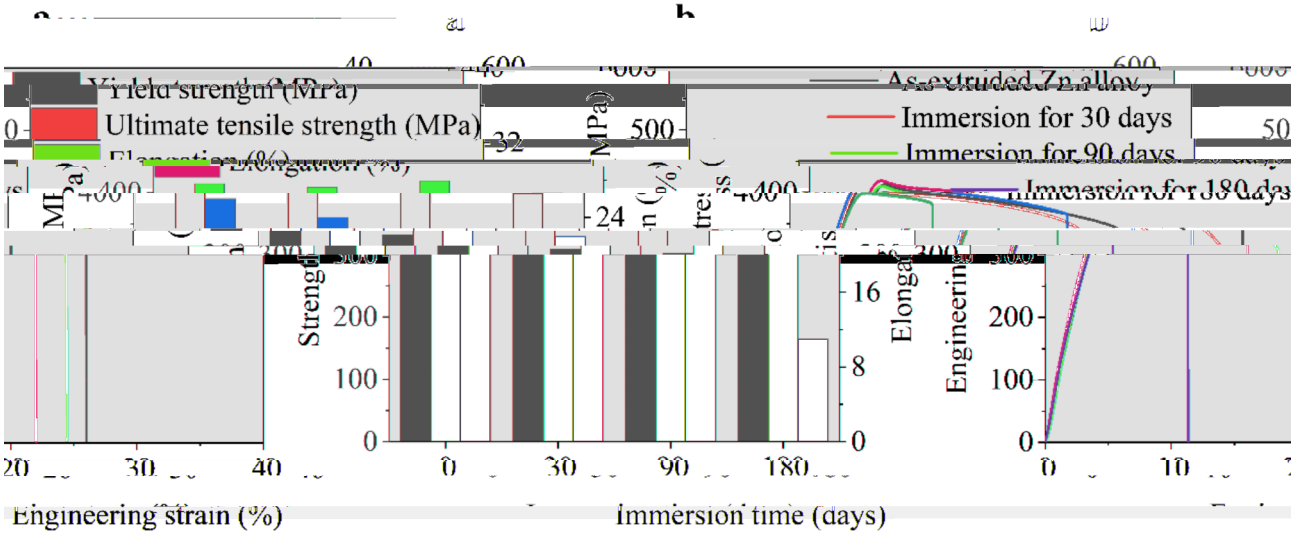

Fig. 7. Mechanical properties of as-extruded Zn alloys after immersion. (**a**) Typical tensile curves. (**b**) Comparison of as-extruded Zn alloys immersed for different time.

cell activity remained consistent after 3 and 7 days. It is worth mentioning that RMSC cells exhibited higher cell activity than C3H10 cells at all Zn alloy extract concentrations.

Figure 9 illustrates the ALP staining morphology and osteogenic activity of C3H10 cells co-cultured with a 50% concentration of Ti and Zn alloy extract for 7 days. The presence of blue-violet crystals with varying color gradients and areas was observed in Ti and Zn alloy groups. Notably, Zn alloy group exhibited darker and more extensive regions of blue-violet crystals compared to Ti group, suggesting that Zn alloys have a superior ability to promote bone mineralization. Consistent with this observation, the bar graph depicting ALP activity further confirmed that Zn alloys have a higher activity in C3H10 cells after 7 days of co-culture with different extracts. Additionally, the bone-enhancing properties of the Zn alloys were evaluated using alizarin red staining. The staining plots revealed a significant increase in the percentage of red crystalline regions after 14 days of culture. This trend was further supported by the histograms, which demonstrated a consistent increase in activity for Zn alloys.

Discussion

As-extruded Zn-0.8Mg-0.2Mn alloy has a remarkable UTS of 414 MPa, which is higher than that of the developed Zn-Mg-Mn alloys, as listed in Table 3. High strength of the studied alloy is intricately linked to microstructures, including grain size, precipitates, and refined Mg_2Zn_{11} particles. Firstly, the reduction in grain size of the as-extruded Zn-Mg-Mn alloy results in a notable increase in grain boundary density. In polycrystalline materials, grain boundaries play a pivotal role in impeding dislocation movement. Grain boundary strengthening effect is described by the Hall-Petch formula, $\sigma_y = \sigma_0 + kd^{-\frac{1}{2}}$, wherein the strength increase is inversely proportional to the reciprocal of the square root of the grain size[34]. The strength contribution from grain refinement is calculated to 231 MPa after taking k value as 580 MPa μm1/2[35]. Secondly, the transformation of the lamellar eutectic structure into a granular phase enhances the strengthening effect of the second phase[36]. During the tensile process, while the soft Zn matrix undergoes plastic deformation, the hard Mg_2Zn_{11}phase remains in the elastic stage. As strain increases, a substantial number of dislocations are generated in the soft phase, augmenting its strength, thereby adapting the mechanical properties to those of the hard phase[37,38]. Moreover, in Zn alloys, the presence of fine and diffuse particle phases promotes plastic deformation of more Zn grains, consequently enhancing the overall strength of the Zn alloys. As illustrated in Fig. 1b, the particle phase size is smaller than that of the Zn grains, approximately 0.5 μm. The volume fraction of Mg_2Zn_{11} particles is 14.6% on the basis of Zn-Mg phase diagram. The strength contribution (σ_s) from fine Mg_2Zn_{11} particles is calculated by the equation: $\sigma_s = \frac{0.84Gb}{2\pi(1-v)^{1/2}\lambda} ln\frac{r}{2b}$, where λ and r are the inter-particle space and average size of particle phases. Thus, it can be calculated that σ_s is 47 MPa. Lastly, the presence of numerous nano-sized precipitates in the as-extruded Zn alloy impedes the movement of dislocations. The Orowan mechanism elucidates the interaction between the precipitates and dislocations, wherein the dislocation encounters the precipitates, leading to the formation of dislocation loops. This process results in an increase in dislocation density and, consequently, an enhancement in strength[39–41].The rest strength contribution from is precipitation strengthening, which is attributed to formation of nano-sized $MnZn_{13}$ phases. In a word, the developed Zn-Mg-Mn alloy has a high strength that is achieved in various strengthening modes. And grain boundary strengthening plays a dominant role in strength contributions.

In addition to high strength, as-extruded Zn-Mg-Mn alloy has a moderate elongation, which meets the mechanical requirement of biodegradable metals. Due to the hexagonal close-packed (HCP) crystal structure

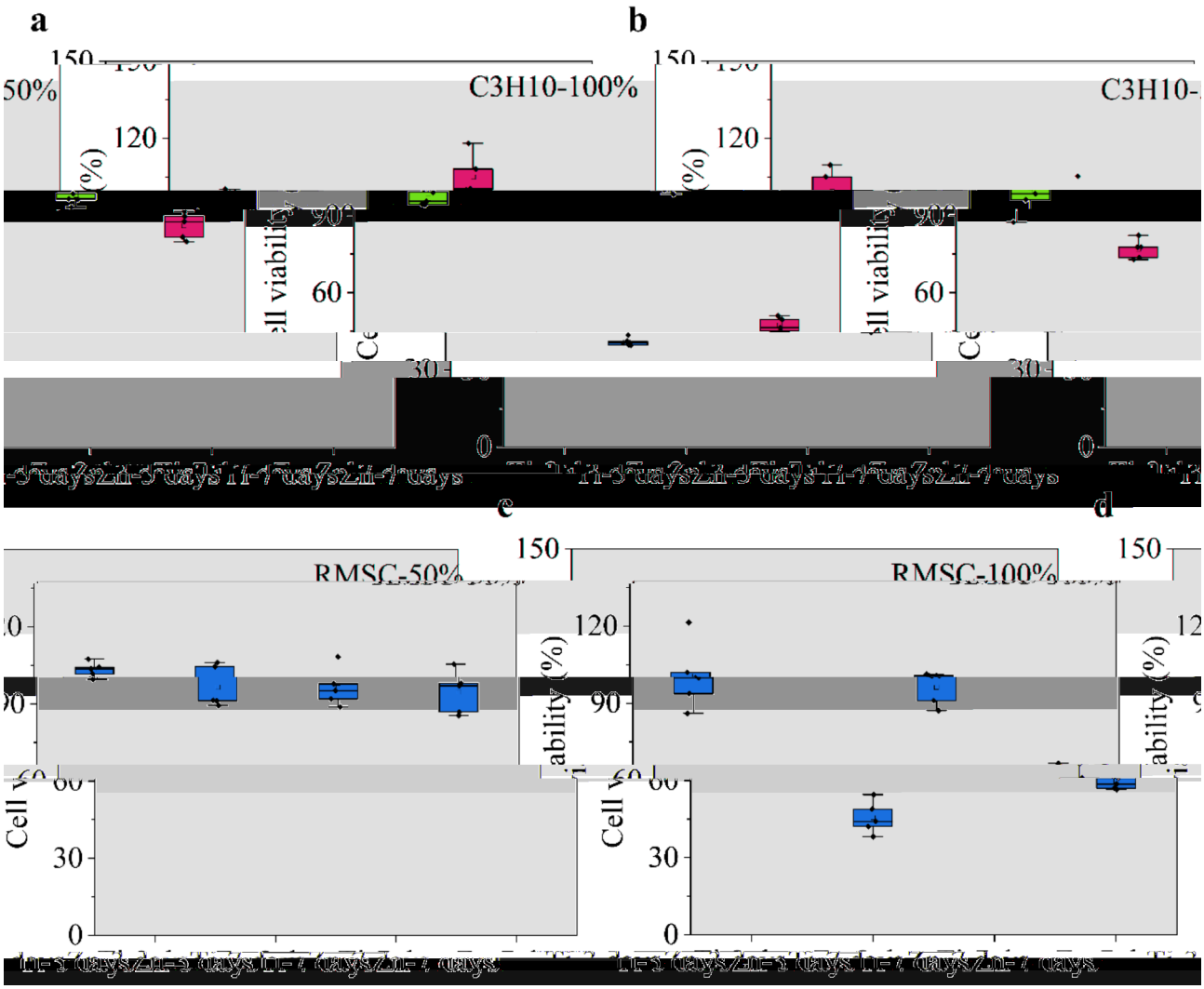

Fig. 8. Cell viability of C3H10 and RMSC cells after culturing with 100% and 50% extracts. (**a**) Cell viability of C3H10 cell after culturing with 100% extracts. (**b**) Cell viability of C3H10 cell after culturing with 50% extracts. (**c**) Cell viability of RMSC cell after culturing with 100% extracts. (**d**) Cell viability of RMSC cell after culturing with 50% extracts.

of Zn, the number of independent slip systems that accumulate plastic deformation at room temperature is less than five. Earlier literature has reported that the deformation modes of Zn alloys may involve non-basal dislocation slip and twinning[28,48,49]. In order to explain the elongation of as-extruded Zn-Mg-Mn alloy, Schmid factors (SF) of various deformation modes were analyzed, as shown in Fig. 10. Among dislocation slipping, SF of basal and prismatic $<\mathbf{a}>$ dislocation is lower than pyramidal $<\mathbf{a}>$ and $<\mathbf{c}+\mathbf{a}>$ dislocation, further demonstrated non-basal dislocation slip. Additionally, the SF values for $<\mathbf{c}+\mathbf{a}>$ dislocations and twins closely resemble those of prismatic dislocations, signifying that as-extruded Zn alloy has a sufficiently large number of independent slip systems at room temperature. Consequently, with multiple deformation modes, the as-extruded Zn alloys exhibit high elongation exceeding 25% in room temperature tensile tests. However, the immersion of Zn alloys in Hank's solution results in surface damage and the formation of corrosion pits of various sizes. It is widely recognized that the elongation of metallic materials is intimately linked to surface defects. Shi et al. also highlighted that the surface roughness of Zn alloys influences the elongation of Zn-Cu alloys[50]. Thus, the corrosion pits generated during the corrosion process serve as additional crack sources and promote crack extension, ultimately leading to a reduction in elongation. The degradation of mechanical properties of biodegradable Zn alloys plays a critical role in healing. It has been reported that an ideal biodegradable metal can maintain mechanical properties according to the repair cycle of the damaged tissues/organics. In general, the mechanical integrity of degradable metals needs to be maintained for 3–6 months[29]. Then, biodegradable metals are gradually degraded and completely removed and excreted from the body after the function of the tissue or organ is restored. The as-extruded Zn-Mg-Mn alloy has a suitable mechanical integrity, showing no degradation of strength. Although the elongation is gradually decreased, it is still higher than 10% even after degradation for

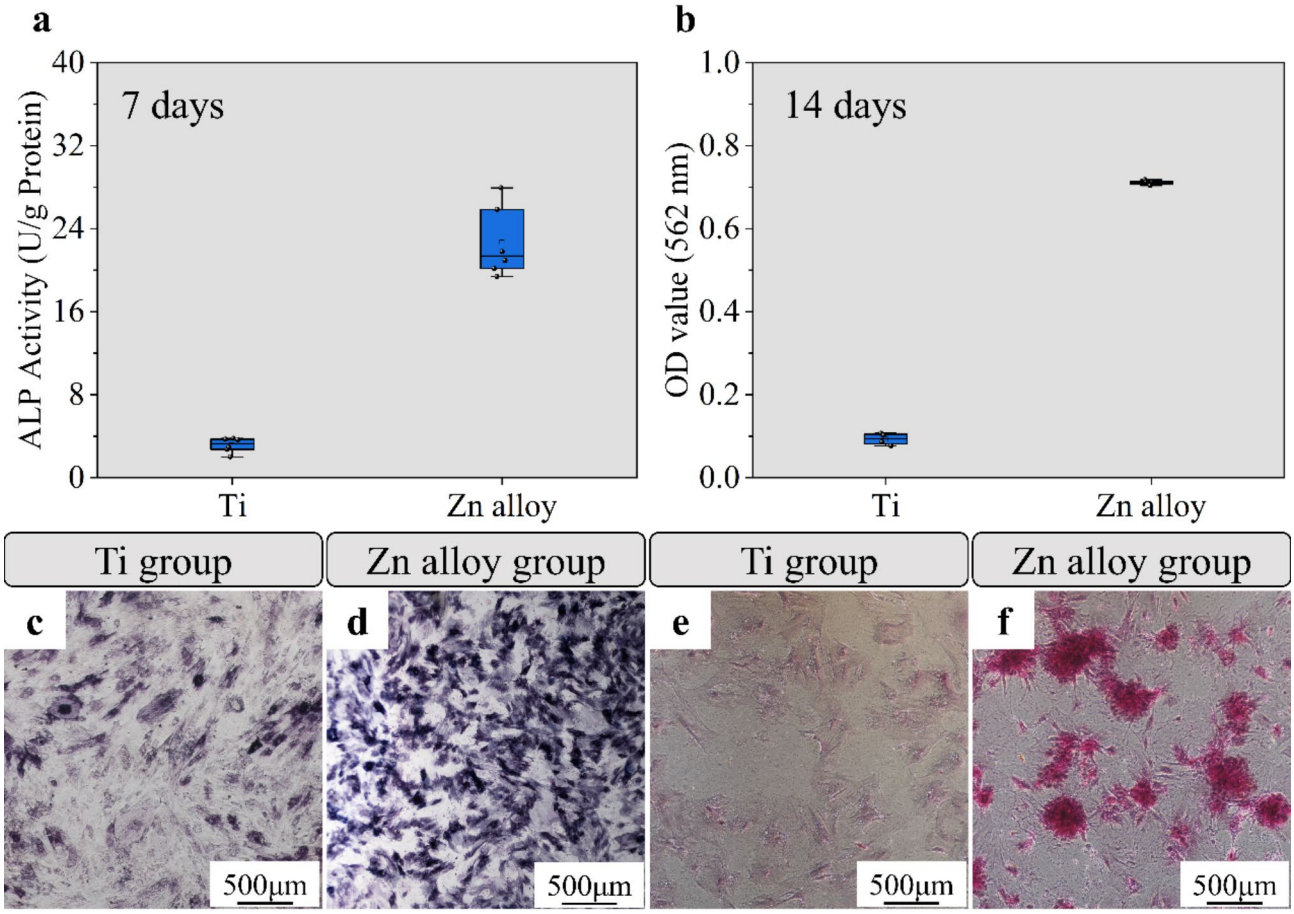

Fig. 9. Osteogenic properties of as-extruded Zn alloys. (**a**) ALP osteogenic activity of C3H10 cells after co-culturing with 50% extracts for 7 days. (**b**) Alizarin red osteogenic activity of C3H10 cells after co-culturing with 50% extracts for 14 days. (**c**,**d**) ALP staining images. (**e**,**f**) ARS images.

Alloys (wt%)	Processing state	UTS (MPa)	Elongation (%)	Reference
Zn-0.8Mn-0.4Mg	Extrusion (230 ℃)	359	5	42
Zn-0.8Mn-0.1Mg	Extrusion (200 ℃)	355	19	43
Zn-0.8Mn-1Mg		359	8	
Zn-0.6Mn-0.05Mg	Extrusion (230 ℃)	345	28	33
Zn-0.8Mn-0.05Mg		356	20	
Zn-0.2Mg-0.1Mn	Extrusion (200 ℃)	266	23	27
Zn-0.2Mg-0.3Mn		300	27	
Zn-0.2Mg-0.5Mn		338	30	
Zn-0.2Mg-0.8Mn		383	21	
Zn-0.2Mg-0.8Mn	Extrusion (150 ℃)	372	33	28
	Extrusion (200 ℃)	380	21	
	Extrusion (250 ℃)	360	19	
	Extrusion (300 ℃)	360	11	
Zn-0.6Mg-0.1Mn	ECAP (150 ℃)	358	23	44
Zn-0.1Mg-0.02Mn	Rolling (25 ℃)	380	16	45
Zn-0.05Mg-0.1Mn	Rolling (25 ℃)	274	41	46
Zn-1Mg-0.1Mn	Rolling (250 ℃)	299	26	47
Zn-0.8Mg-0.2Mn	Extrusion (150 ℃)	414	26	This work

Table 3. Mechanical properties of the developed Zn-Mg-Mn alloys.

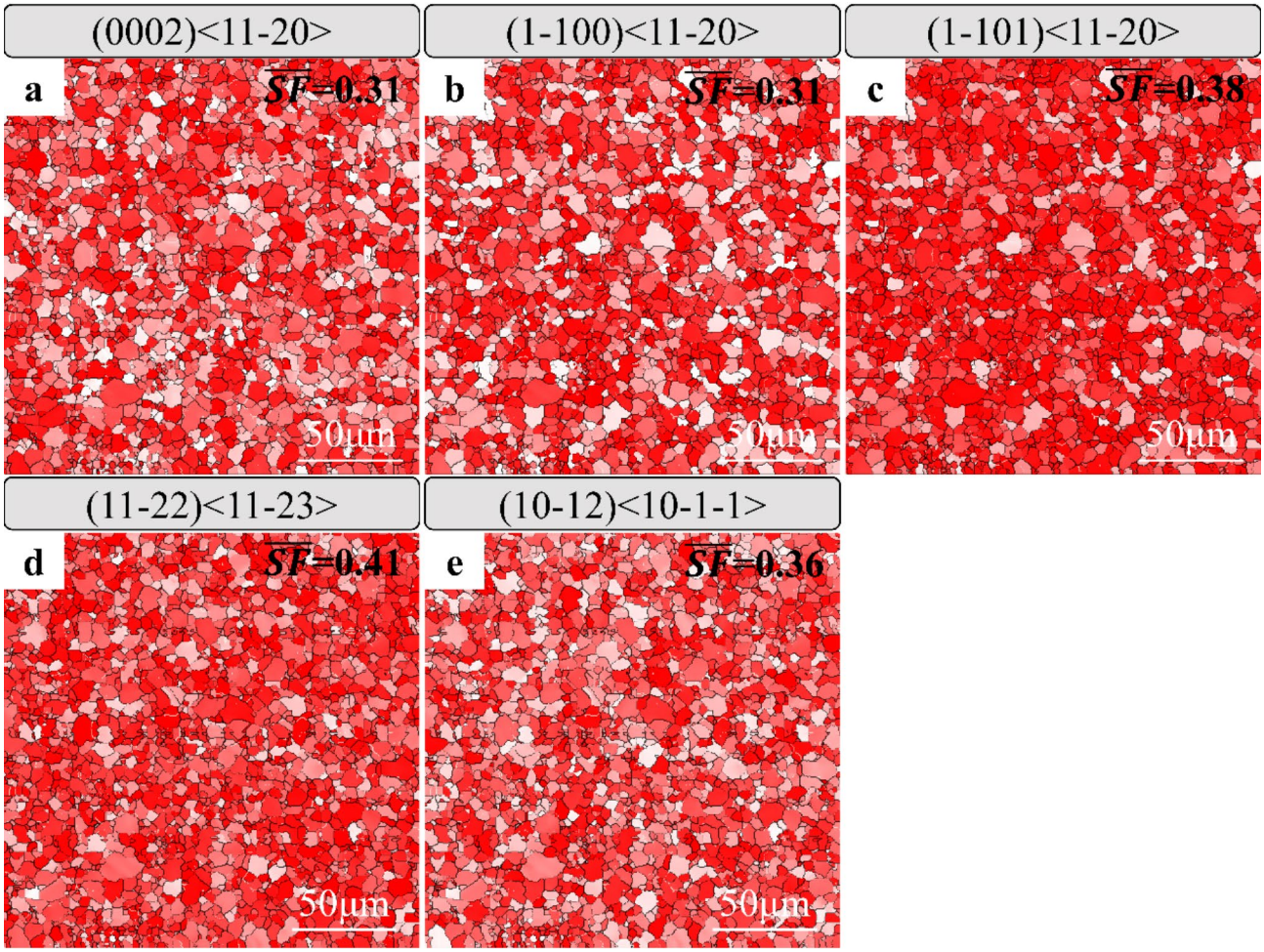

Fig. 10. SF of different slip systems in Zn alloys. (**a**) Basal, (**b**) prismatic, and (**c**) pyramidal slip systems with **a** Burgers vector. (**d**) < **c** + **a** > dislocations. (**e**) Twinning.

6 months. The elongation of Zn alloy after immersion for 6 months is enough for some orthopeadic implants, such as screws or bone plates.

The surface corrosion morphology of as-extruded Zn alloys exhibits distinct changes over varying immersion times. Initially, upon immersion, a corrosion layer forms on the surface of the Zn alloy due to direct exposure to the solution. Chloride ions present in the solution infiltrate this corrosion layer, inducing further corrosion of the Zn alloy. Subsequent removal of corrosion products reveals the emergence of minute pitting pits on the alloy surface. The localized protocell structure formed between the Mg_2Zn_{11} particle phase and Zn grains, owing to potential differences, facilitates localized corrosion, leading to the appearance of small-sized pitting pits within the refined eutectic organization. Additionally, TEM analysis has confirmed the presence of nanoscale precipitated phases within the Zn grains, further promoting the formation of these small-sized corrosion pits. As immersion time progresses, chloride ion attack on the corrosion layer intensifies, augmenting the number and diameter of pitting pits. Penetration of the corrosive medium into pre-existing pits exacerbates localized corrosion, leading to pit enlargement. With an increasing number of pits reaching a critical threshold, nearby pits coalesce, giving rise to larger pits. Ultimately, after a 180-day immersion period, the surface of the as-extruded Zn alloy exhibits the presence of large pitting pits with significant depth. This outcome is attributed to the combined longitudinal and transverse effects of the corrosive medium on the alloy surface. The corrosion mechanism of the as-extruded Zn alloys in Hank's solution is illustrated in Fig. 11, depicting a progressive increase in the size and number of pitting craters with prolonged immersion, culminating in the formation of large localized corrosion craters.

Conclusions

In this work, the grain size, lamellar Mg_2Zn_{11} phase of Zn-Mg-Mn alloy were refined after extrusion. And nano-sized $MnZn_{13}$ precipitates were distributed along the grain boundaries. The refined microstructures and precipitates contributed in a high strength over 400 MPa, which was higher than that of the reported Zn-Mg-Mn alloys. After immersion, the tensile strength of as-extruded Zn-Mg-Mn alloys remained largely unchanged after varying immersion cycles, a considerable decrease in elongation was observed. This reduction in elongation was primarily attributed to the formation of corrosion pits on the surface, which facilitated crack propagation.

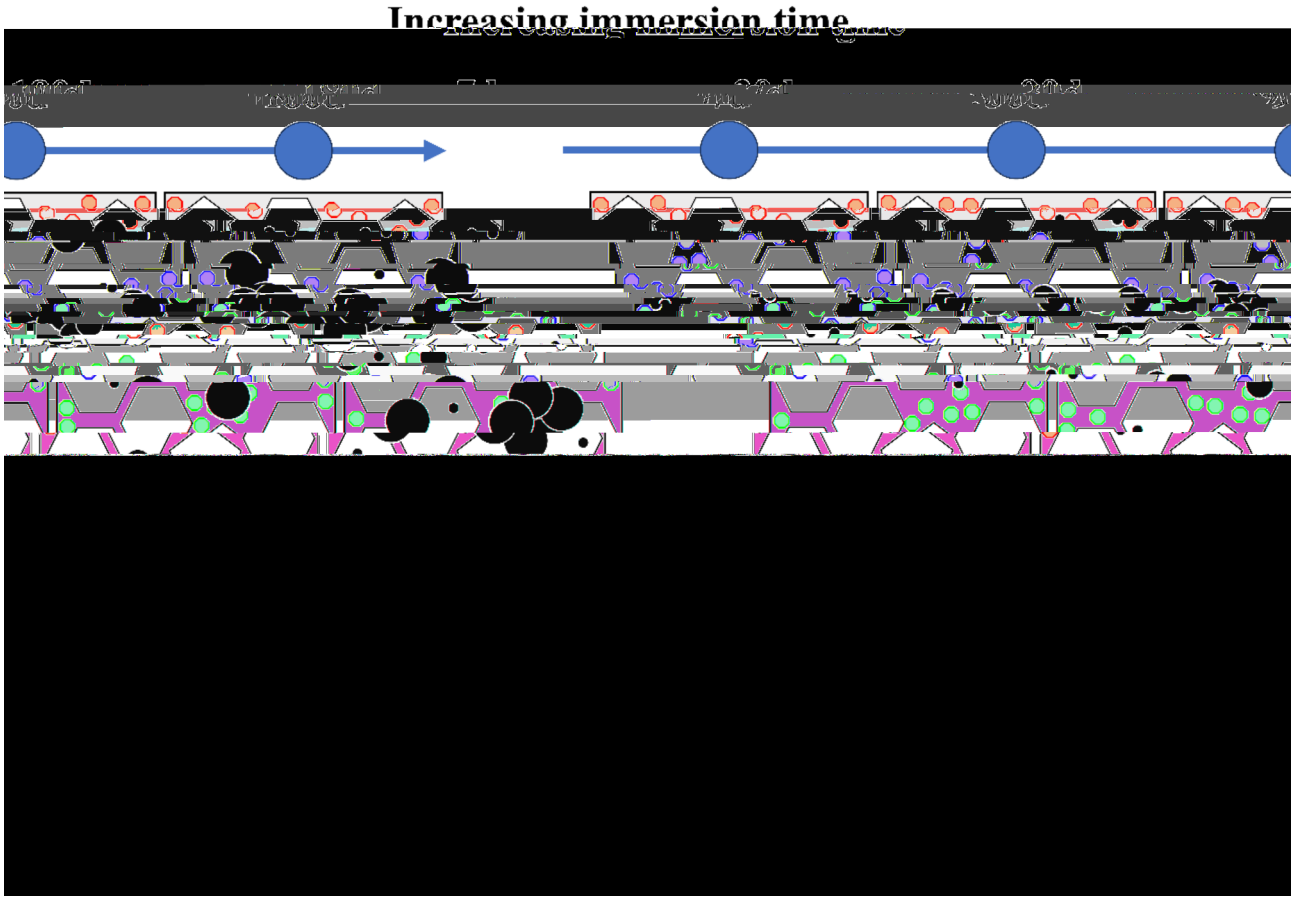

Fig. 11. Corrosion modes of Zn alloys as increasing immersion time.

Biocompatibility tests demonstrated that 50% concentration of Zn alloy extracts cultured with C3H10 and RMSC cells exhibited cellular activity exceeding 80%, indicative of excellent cytocompatibility. Furthermore, ALP and alizarin red staining results revealed that Zn-Mg-Mn alloys displayed promising early and late induced osteogenic properties. These results demonstrated the as-extruded Zn-Mg-Mn alloys have a high strength and suitable mechanical integrity during degradation. It provides evidence that Zn alloys are promising orthopeadic implants in the aspect of mechanical integrity.

Data availability

The datasets used and/or analyzed during the current study available from the corresponding author on reasonable request.

Received: 14 June 2024; Accepted: 4 November 2024
Published online: 19 December 2024

References

1. Bowen, P. K., Drelich, J. & Goldman, J. Zinc exhibits ideal physiological corrosion behavior for bioabsorbable stents. *Adv. Mater.* **25**, 2577–2582. https://doi.org/10.1002/adma.201300226 (2013).
2. Yang, H. et al. Evolution of the degradation mechanism of pure zinc stent in the one-year study of rabbit abdominal aorta model. *Biomater* **145**, 92–105. https://doi.org/10.1016/j.biomaterials.2017.08.022 (2017).
3. Yang, N., Venezuela, J., Almathami, S. & Dargusch, M. Zinc-nutrient element based alloys for absorbable wound closure devices fabrication: Current status, challenges, and future prospects. *Biomater* **280**, 121301. https://doi.org/10.1016/j.biomaterials.2021.121301 (2022).
4. Jia, B. et al. High-strength biodegradable zinc alloy implants with antibacterial and osteogenic properties for the treatment of MRSA-induced rat osteomyelitis. *Biomater* **287**, 121663. https://doi.org/10.1016/j.biomaterials.2022.121663 (2022).
5. Zhang, W. et al. Appropriately adapted properties of hot-extruded Zn-0.5Cu-xFe alloys aimed for biodegradable guided bone regeneration membrane application. *Bioact Mater.* **6**, 975–989. https://doi.org/10.1016/j.bioactmat.2020.09.019 (2021).
6. Drelich, A. J., Zhao, S., Guillory, R. J. 2nd, Drelich, J. W., Goldman, J. & nd, & Long-term surveillance of zinc implant in murine artery: Surprisingly steady biocorrosion rate. *Acta Biomater.* **58**, 539–549. https://doi.org/10.1016/j.actbio.2017.05.045 (2017).
7. Guo, H. et al. In vitro and in vivo studies of biodegradable Zn-Li-Mn alloy staples designed for gastrointestinal anastomosis. *Acta Biomater.* **121**, 713–723. https://doi.org/10.1016/j.actbio.2020.12.017 (2021).
8. Werkhoven, R. J., Sillekens, W. H. & van Lieshout, J. B. J. M. In *Magnesium Technology 2011* (eds Sillekens, W. H., Agnew, S. R., Neelameggham, N. R., Suveen, N. & Mathaudhu) 419–424 (Springer, 2016).

9. Srinivasarao, B., Zhilyaev, A. P., Langdon, T. G. & Pérez-Prado, M. T. On the relation between the microstructure and the mechanical behavior of pure Zn processed by high pressure torsion. *Mater. Sci. Eng. A* **562**, 196–202. https://doi.org/10.1016/j.msea.2012.11.027 (2013).
10. Pieła, K. et al. Zinc subjected to plastic deformation by complex loading and conventional extrusion: Comparison of the microstructure and mechanical properties. *Mater. Des.* **117**, 111–120. https://doi.org/10.1016/j.matdes.2016.12.056 (2017).
11. Shi, Z. Z. et al. Design biodegradable zn alloys: Second phases and their significant influences on alloy properties. *Bioact Mater.* **5**, 210–218. https://doi.org/10.1016/j.bioactmat.2020.02.010 (2020).
12. Bednarczyk, W. et al. Determination of critical resolved shear stresses associated with <a> slips in pure zn and Zn-Ag alloys via micro-pillar compression. *Mater. Des.* **229**. https://doi.org/10.1016/j.matdes.2023.111897 (2023).
13. Pachla, W. et al. Structural and mechanical aspects of hypoeutectic Zn-Mg binary alloys for biodegradable vascular stent applications. *Bioact Mater.* **6**, 26–44. https://doi.org/10.1016/j.bioactmat.2020.07.004 (2021).
14. Tong, X. et al. Development of biodegradable Zn-1Mg-0.1RE (RE = Er, Dy, and Ho) alloys for biomedical applications. *Acta Biomater.* **117**, 384–399. https://doi.org/10.1016/j.actbio.2020.09.036 (2020).
15. Hernández-Escobar, D. et al. Effect of post-deformation annealing on the microstructure and micro-mechanical behavior of Zn–Mg hybrids processed by high-pressure torsion. *Mater. Sci. Eng. A* **771**. https://doi.org/10.1016/j.msea.2019.138578 (2020).
16. Wang, X., Ma, Y., Meng, B. & Wan, M. Effect of equal-channel angular pressing on microstructural evolution, mechanical property and biodegradability of an ultrafine-grained zinc alloy. *Mater. Sci. Eng. A* **824**. https://doi.org/10.1016/j.msea.2021.141857 (2021).
17. Mostaed, E. et al. Novel Zn-based alloys for biodegradable stent applications: Design, development and in vitro degradation. *J. Mech. Behav. Biomed. Mater.* **60**, 581–602. https://doi.org/10.1016/j.jmbbm.2016.03.018 (2016).
18. Wang, L. Q. et al. Microstructure, mechanical properties and fracture behavior of As-extruded Zn–Mg binary alloys. *Acta Metall. Sin* **30**, 931–940. https://doi.org/10.1007/s40195-017-0585-4 (2017).
19. Huang, H. et al. A high-strength and biodegradable Zn–Mg alloy with refined ternary eutectic structure processed by ECAP. *Acta Metall. Sin* **33**, 1191–1200. https://doi.org/10.1007/s40195-020-01027-x (2020).
20. Hybasek, V. et al. Influence of model environment complexity on corrosion mechanism of biodegradable zinc alloys. *Corro Sci.* **187**. https://doi.org/10.1016/j.corsci.2021.109520 (2021).
21. Gong, H., Wang, K., Strich, R. & Zhou, J. G. In vitro biodegradation behavior, mechanical properties, and cytotoxicity of biodegradable Zn-Mg alloy. *J. Biomed. Mater. Res. B Appl. Biomater.* **103**, 1632–1640. https://doi.org/10.1002/jbm.b.33341 (2015).
22. Ye, L. et al. Effect of grain size and volume fraction of eutectic structure on mechanical properties and corrosion behavior of as-cast Zn–Mg binary alloys. *J. Mater. Res. Technol.* **16**, 1673–1685. https://doi.org/10.1016/j.jmrt.2021.12.101 (2022).
23. Kubasek, J. et al. Structure, mechanical characteristics and in vitro degradation, cytotoxicity, genotoxicity and mutagenicity of novel biodegradable Zn-Mg alloys. *Mater. Sci. Eng. C* **58**, 24–35. https://doi.org/10.1016/j.msec.2015.08.015 (2016).
24. Sun, S. et al. Abnormal effect of Mn addition on the mechanical properties of as-extruded Zn alloys. *Mater. Sci. Eng. A* **701**, 129–133. https://doi.org/10.1016/j.msea.2017.06.037 (2017).
25. Shi, Z. Z., Yu, J. & Liu, X. F. Microalloyed Zn-Mn alloys: From extremely brittle to extraordinarily ductile at room temperature. *Mater. Des.* **144**, 343–352. https://doi.org/10.1016/j.matdes.2018.02.049 (2018).
26. Shi, Z. Z., Yu, J. & Liu, X. F. Twinning in MnZn13 intermetallic compound with base-centered monoclinic structure in Zn-0.75Mn alloy. *Mater. Charact.* **137**, 9–13. https://doi.org/10.1016/j.matchar.2018.01.021 (2018).
27. Wang, L. et al. Effect of Mn content on the microstructure and mechanical properties of as-extruded Zn-0.2Mg-Mn (wt%) alloys. *Mater. Charact.* **194**, 112400. https://doi.org/10.1016/j.matchar.2022.112400 (2022).
28. Lou, D., Wang, L., Ren, Y., Li, H. & Qin, G. Textural evolution and improved ductility in Zn-0.2Mg-0.8Mn (wt%) alloys at different extrusion temperatures. *J. Alloy Compd.* **860**. https://doi.org/10.1016/j.jallcom.2020.158530 (2021).
29. Zheng, Y. F., Gu, X. N. & Witte, F. Biodegradable metals. *Mater. Sci. Eng. R* **77**, 1–34. https://doi.org/10.1016/j.mser.2014.01.001 (2014).
30. Liu, H. et al. Evolution of Mg–Zn second phases during ECAP at different processing temperatures and its impact on mechanical properties of Zn-1.6Mg (wt.%) alloys. *J. Alloy Compd.* **811**. https://doi.org/10.1016/j.jallcom.2019.151987 (2019).
31. Mostaed, E., Sikora-Jasinska, M., Drelich, J. W. & Vedani, M. Zinc-based alloys for degradable vascular stent applications. *Acta Biomater.* **71**, 1–23. https://doi.org/10.1016/j.actbio.2018.03.005 (2018).
32. Aslam, R. In *Electrochemical and Analytical Techniques for Sustainable Corrosion Monitoring* (eds Jeenat Aslam, Chandrabhan Verma, & Chaudhery Mustansar Hussain) 25–37 (Elsevier, 2023).
33. Shi, Z. Z. et al. 300 MPa grade biodegradable high-strength ductile low-alloy (BHSDLA) Zn-Mn-Mg alloys: An in vitro study. *J. Mater. Sci. Technol.* **138**, 233–244. https://doi.org/10.1016/j.jmst.2022.08.015 (2023).
34. Figueiredo, R. B., Kawasaki, M. & Langdon, T. G. Seventy years of Hall-Petch, ninety years of superplasticity and a generalized approach to the effect of grain size on flow stress. *Prog Mater. Sci.* **137**. https://doi.org/10.1016/j.pmatsci.2023.101131 (2023).
35. Liu, Z., Qiu, D., Wang, F., Taylor, J. A. & Zhang, M. Effect of grain refinement on Tensile properties of cast zinc alloys. *Metall. Mater. Trans. A* **47**, 830–841. https://doi.org/10.1007/s11661-015-3229-1 (2015).
36. Huang, K., Marthinsen, K., Zhao, Q. & Logé, R. E. The double-edge effect of second-phase particles on the recrystallization behaviour and associated mechanical properties of metallic materials. *Prog Mater. Sci.* **92**, 284–359. https://doi.org/10.1016/j.pmatsci.2017.10.004 (2018).
37. Zhu, Y. & Wu, X. Perspective on hetero-deformation induced (HDI) hardening and back stress. *Mater. Res. Lett.* **7**, 393–398. https://doi.org/10.1080/21663831.2019.1616331 (2019).
38. Du, X. H. et al. Dual heterogeneous structures lead to ultrahigh strength and uniform ductility in a co-cr-ni medium-entropy alloy. *Nat. Commun.* **11**, 2390. https://doi.org/10.1038/s41467-020-16085-z (2020).
39. Peng, S., Wang, Z., Li, J., Fang, Q. & Wei, Y. Beyond Orowan hardening: Mapping the four distinct mechanisms associated with dislocation-precipitate interaction. *Int. J. Plast.* **169**, 103710. https://doi.org/10.1016/j.ijplas.2023.103710 (2023).
40. Poole*, W. J., Wang, X., Lloyd, D. J. & Embury, J. D. The shearable–non-shearable transition in Al–Mg–Si–Cu precipitation hardening alloys: Implications on the distribution of slip, work hardening and fracture. *Phil Mag* **85**, 3113–3135. https://doi.org/10.1080/14786430500154935 (2005).
41. Krasnikov, V. S., Mayer, A. E. & Pogorelko, V. V. Prediction of the shear strength of aluminum with θ phase inclusions based on precipitate statistics, dislocation and molecular dynamics. *Int. J. Plast.* **128**, 102672. https://doi.org/10.1016/j.ijplas.2020.102672 (2020).
42. Sun, J. et al. Development of a high-strength Zn-Mn-Mg alloy for ligament reconstruction fixation. *Acta Biomater.* **119**, 485–498. https://doi.org/10.1016/j.actbio.2020.10.032 (2021).
43. Yu, X. et al. Study on mechanical and degradation behavior of Zn–Mn-xMg alloys under coupling effects of stress and SBF. *J. Mater. Res. Technol.* **28**, 3960–3975. https://doi.org/10.1016/j.jmrt.2024.01.012 (2024).
44. Huang, H. et al. Multi-interactions of dislocations and refined microstructure in a high strength and toughness Zn-Mg-Mn alloy. *J. Mater. Res. Technol.* **9**, 14116–14121. https://doi.org/10.1016/j.jmrt.2020.09.126 (2020).
45. Li, J. et al. Grain refinement mechanism and mechanical properties of wrought Zn-0.1Mg-0.02Mn alloys by rolling at different reductions. *J. Mater. Res. Technol.* **25**, 6263–6274. https://doi.org/10.1016/j.jmrt.2023.07.093 (2023).
46. Ardakani, M. S., Mostaed, E., Sikora-Jasinska, M., Kampe, S. L. & Drelich, J. W. The effects of alloying with Cu and Mn and thermal treatments on the mechanical instability of Zn-0.05Mg alloy. *Mater. Sci. Eng. A*. **770**. https://doi.org/10.1016/j.msea.2019.138529 (2020).

47. Liu, X. et al. Micro-alloying with mn in Zn–Mg alloy for future biodegradable metals application. *Mater. Des.* **94**, 95–104. https://doi.org/10.1016/j.matdes.2015.12.128 (2016).
48. Liu, S., Kent, D., Doan, N., Dargusch, M. & Wang, G. Effects of deformation twinning on the mechanical properties of biodegradable Zn-Mg alloys. *Bioact Mater.* **4**, 8–16. https://doi.org/10.1016/j.bioactmat.2018.11.001 (2019).
49. Sun, S., Liu, J. & Lou, D. Microstructure evolution of as-extruded Zn–0.62Mn alloys during room temperature compression. *Mater. Sci. Technol.* **37**, 930–934. https://doi.org/10.1080/02670836.2021.1964691 (2021).
50. Shi, Z. Z., Meng, L., Li, X. & Wang, L. Surface roughness-induced plasticity (SRIP) in a biodegradable zn Alloy. *Adv. Mater.* **35**. https://doi.org/10.1002/adma.202207570 (2022).

Acknowledgements

This work was supported by Joint Fund Project for Science and Technology Innovation (2021Y9023), Major Scientific Research Project of Fujian Province (2021ZD01003), Joint Project for Health and Education of Fujian Province (2019-WJ-01), Health Research Personnel Training Project of Fujian Provincial Health Commission (2019-CX-1), Science and Technology Planning Project of Fujian Province (2019J01173), Startup Fund for Scientific Research of Fujian Medical University (2020QH2050), Postdoctoral Science Foundation of China (2022M710702), Postdoctoral start-up fund of Fujian Provincial Hospital (0080132201), Fujian Provincial Natural Science Foundation Projects (2020J05270), The Flint Fund project (2020HSJJ20), Sponsored by Fujian provincial health technology project (2020QNA009).

Author contributions

L.CW. and S.C. wrote the main manuscript text, Y.YL prepared development or design of methodology, Y.LH and Z.W conducted a research and investigation process, L.FQ and X.YH prepared creation of the published work, specifically data presentation, L.J and X.J acquired the financial support for the project and coordinated responsibility for the research activity planning. All authors reviewed the manuscript. Chengwu Lu, Chao Song and Yunlong Yu contributed to the work equally and should be regarded as co-first authors. Jun Luo and Jie Xu contributed to the work equally and should be regarded as co-corresponding authors.

Declarations

Competing interests

The authors declare no competing interests.

Additional information

Correspondence and requests for materials should be addressed to J.L. or J.X.